



CHORUS

This is the accepted manuscript made available via CHORUS. The article has been published as:

Low-Temperature Band Transport and Impact of Contact Resistance in Organic Field-Effect Transistors Based on Single-Crystal Films of Ph-BTBT-C10

Joung-min Cho and Takehiko Mori

Phys. Rev. Applied **5**, 064017 — Published 29 June 2016

DOI: [10.1103/PhysRevApplied.5.064017](https://doi.org/10.1103/PhysRevApplied.5.064017)

Low-temperature band transport and impact of contact resistance in crystalline organic transistors using Ph-BTBT-C10

Joung-min Cho^{1,2,a)} and Takehiko Mori^{1,3}

¹*Department of Organic and Polymeric Materials, Tokyo Institute of Technology, 2-12-1 Ookayama, Tokyo 152-8552, Japan*

²*Present address: Display R&D Group in Mobile Communications Business, Samsung Electronics, Suwon-si, Gyeonggi-do 16677, Republic of Korea*

³*ACT-C, JST, Honcho, Kawaguchi, Saitama 332-0012, Japan*

Transistors based on single crystalline films of 2-decyl-7-phenyl-[1]benzothieno[3,2-b][1]benzothiophene (Ph-BTBT-10) fabricated using the blade-coating method are investigated by the four-probe method down to low temperatures. The four-probe mobility is as large as 18 cm²/Vs at room temperature, and increases to 45 cm²/Vs at 80 K. At 60 K the two-probe mobility drops abruptly by about 50%, but the mobility drop is mostly attributed to the increase of the source resistance. The carrier transport in the present single crystalline film is regarded as essentially band-like down to 30 K.

^{a)}Author to whom correspondence should be addressed. Electric mail: joungmin.cho@samsung.com

I. INTRODUCTION

The emergence of solution-processable high-performance organic semiconductors has opened a new era of organic transistors for printed electronics applications.¹⁻⁷ There have been found excellent small-molecule semiconductors that realize high mobilities beyond $1 \text{ cm}^2/\text{Vs}$ corresponding to the value of amorphous silicon transistors.⁸⁻¹⁰ High solubility has been attained by alkyl substitution in such materials as 6,13-bis(triisopropylsilylethynyl) (TIPS)-pentacene and 2,7-dialkyl-benzothienobenzothiophene (C_n -BTBT), where high performance has been realized in the solution-processed transistors.¹¹⁻¹³ In particular, organic transistors using single-crystalline films fabricated by solution coating or inkjet printing achieve mobilities above $10 \text{ cm}^2/\text{Vs}$.⁵⁻⁷ Although the alkyl chain increases solubility, it also decreases melting points of materials, which are critical for thermal stability of the resulting devices.¹⁴ Recently, an asymmetric organic semiconductor, 2-decyl-7-phenyl-[1]benzothieno[3,2-b][1]benzothiophene (Ph-BTBT-10), has drawn attention owing to the thermal stability and the device reliability as well as the high mobility of $13.9 \text{ cm}^2/\text{Vs}$ and the solution processability.¹⁵⁻¹⁷

Solution-processed organic single-crystal transistors have also paved the way for studying intrinsic transport properties of organic semiconductors. A typical technique to make organic single-crystal transistors is placing grown crystals onto substrates.¹⁸⁻²⁰ Single-crystal transistors have shown high mobility and band-like temperature dependence, where the mobility increases with decreasing the temperature.²¹⁻²⁵ Recently, it has become evident that solution-processed single-crystal transistors have exhibited band-like transport as well.²⁶⁻³⁰ However, the band-like transport generally persists only down to $150 \text{ K} \sim 200 \text{ K}$, which is replaced by the hopping transport at lower temperatures due to the unavoidable extrinsic effect at the interface.¹⁹ It has been reported that the mobility of a TIPS-pentacene transistor continues to increase down to helium temperatures when V_D is sufficiently large.²⁶ Mobilities

of high-quality anthracene and naphthalene crystals measured by the time-of-flight method show a remarkable two-order increase to above $100 \text{ cm}^2/\text{Vs}$ at liquid helium temperatures.³¹ Therefore, it has been a great challenge in organic field-effect transistors for a long time to attain band-like transport persisting down to helium temperatures. Recently, we have reported band-like transport down to 20 K using a solution-grown C8-BTBT crystal with carbon contacts, though the mobility shows an abrupt drop at 80 K.³⁰ The drop has been analyzed in view of the appearance of discrete trap states based on the shoulder structure in the transfer curve.^{32,33} However, in order to investigate the intrinsic transport mechanism, the four-probe measurement is desirable; the four-probe measurements for single-crystal transistors have been previously reported in a few limited cases.^{21,23,34–38} Since the as-grown C8-BTBT crystal is too small, here we have attempted to use the blade-coated crystalline film for the four-probe measurement.

In this paper, we report investigation of charge transport and contact effect in organic single-crystal transistors based on Ph-BTBT-C10 at low temperatures. Thanks to the high quality crystalline film having large single domain over several hundred micrometers long, we can achieve the four-probe measurement using a single crystalline film. Band-like transport is observed down to 80 K, where the four-probe mobility increases to $45 \text{ cm}^2/\text{Vs}$. An abrupt mobility drop appears in two-probe mobility at 60 K like our previous C8-BTBT transistors,³⁰ though there is practically no anomaly in the four-probe mobility. From the analysis of the contact resistance at low temperatures, the mobility drop is mostly attributed to the abrupt increase of the source resistance.

II. EXPERIMENT

A. Fabrication of a single crystalline film by the blade-coating method

Ph-BTBT-C10 (Fig.1(a)) was prepared following the published methods.^{15,16} The 0.025 wt% chlorobenzene solution, which was 15 % of the saturated concentration of Ph-BTBT-C10, was prepared as a semiconductor ink. As a shearing blade, a quartz plate was used. Both sides of the quartz plate were coated by Cytop (Asahi glass), and then the edge of the back side was grinded to promote the crystallization of the organic semiconductor (Fig. 1(a)). A silicon wafer with a thermally grown silicon dioxide (100 nm), the capacitance of which was $C = 33.5 \text{ nF/cm}^2$, was used as the substrate. The shearing blade was placed at a height of 50 μm from the substrate tilted by 5° and set to a stage controller (SHOT-302GS, SIGMAKOKI) to control the shearing speed. The speed was optimized to 2 $\mu\text{m/s}$, which was about the equilibrium condition for the crystal growth in the given concentration in the ambient condition. After the semiconductor solution was dropped on a washed Si/SiO₂ (100 nm) substrate, a crystalline film was obtained by blade-coating. The resulting crystalline film was investigated by crossed-nicols polarized optical microscopy and atomic force microscopy (AFM).

B. Four-probe measurements of organic transistor at low temperatures

A bottom-gate top-contact transistor structure was used to characterize Ph-BTBT-C10. In order to measure not only the transistor characteristics but also the contact resistance, we used the four-probe configuration with additional two sense probes.³⁹⁻⁴² The electrodes were patterned with a shadow mask by thermal deposition of Au (30 nm, 1 \AA /s) onto the Ph-BTBT-C10 crystal as depicted in Fig. 1(b). The channel width and length were 400 μm and 190 μm , respectively. The sense probes were located at the 1/3 and 2/3 positions between the source and the drain electrodes, and penetrated less than 10 % of the channel width to minimize the impact on the channel current.^{41,42} The transistor was cooled from 290 K to 30 K with a low-temperature micro prober system (Riko International) and the transfer characteristics with the

sense potentials were measured with an interval of 10 K. The voltage drops at the source and drain resistance were estimated by the conventional methods^{40–42}.

III. RESULTS AND DISCUSSION

A. Single crystalline film of Ph-BTBT-C10

A crystalline film of Ph-BTBT-10 is fabricated by the blade-coating method as shown in Fig. 1(b). Crossed-nicols polarized micrographs of the film reveal that a large area ($\sim 500 \mu\text{m} \times 500 \mu\text{m}$) is in a single domain because the color of the entire film changes from dark to bright on the rotation of the polarizer. The step-and-terrace structure on the film surface is observed by AFM (Figs. 1(c) and 1(d)), where the height of step is ~ 5 nm, which corresponds to one bilayer of Ph-BTBT-C10 (*c*-axis).¹⁷ For comparison, we made a C8-BTBT film by the blade-coating method, and investigated the height of the steps by AFM. As depicted in Fig. 1(c), the height of Ph-BTBT-C10 is about twice larger than C8-BTBT. This is not due to the slight difference of the alkyl chain length but due to the bilayer structure of Ph-BTBT-C10. The thickness of the film is 25 nm, which corresponds to about five units of bilayers. Therefore, we have confirmed that the simple blade-coating method enables the formation of high quality crystalline film where the whole channel region is within a single domain.

B. Transistor performance at room temperature

Organic single-crystal transistors based on Ph-BTBT-C10 show excellent p-channel performance (Fig. 2). The saturation mobility of $\mu_{\text{sat}} = 13 \text{ cm}^2/\text{Vs}$, extracted from the transfer characteristics at $V_{\text{D}} = -15 \text{ V}$ (Fig. 2(a)), is comparable to the previously reported value ($\mu_{\text{max}} = 14.7 \text{ cm}^2/\text{Vs}$).¹⁵ We have measured five transistors, but the mobility value of the blade-coated transistors is highly reproducible because the channel is fabricated on a single domain. Threshold voltages V_{T} at $V_{\text{D}} = -5 \text{ V}$ and -15 V are obtained as $V_{\text{T}} = -30 \text{ V}$ and $V_{\text{T}} =$

-33 V, respectively, from the extrapolation of the $I_D^{1/2}$ plot. The comparatively large threshold voltage is characteristic of the surface charges generated by the blade-coating,¹⁵ though this is partly due to the contribution of the contact resistance.⁴³ This is also reflected to the nonlinear behavior around $V_D \sim 0$ V in the output characteristics (Fig. 2(b)).⁴⁴ It is generally observed that the influence of contact resistance is magnified in high-performance transistors with extremely low channel resistance,³² as indicated by theoretical simulation.⁴⁵

In this work, we have measured the transfer characteristics at moderate source-drain bias to investigate both the saturation and linear regimes. Since I_D follows $I_D \sim V_G^2$ in the saturation regime and $I_D \sim V_G$ in the linear regime, the transconductance (dI_D/dV_G) makes an anomaly at the border (Fig. 2(c)).³² At $V_D = -15$ V, the saturation regime continues nearly up to $V_G = -50$ V in agreement with $V_T + V_D = -48$ V. At $V_D = -5$ V, however, the crossover occurs around $V_G = -40$ V as expected from $V_T + V_D = -38$ V. The crossover is also obvious from the inflection point of the transfer curve around $V_G = -40$ V (Fig. 2(a)).

C. Estimation of the contact and channel resistance from the sense potentials

Source and drain contact resistance in the transistor is estimated by the four-probe measurements.⁴⁰⁻⁴² Figure 3(a) shows a schematic diagram of the four-probe configuration and the potential distribution. Due to the carrier injection and extraction, potential drops, ΔV_S and ΔV_D , occur at the source and drain contacts, respectively. Because we know the voltages, V_1 and V_2 , at the sense probes, the potentials just inside of the source and the drain, V_S' and V_D' , are estimated by extrapolating potential distribution between the two sense probes linearly to the contacts

$$V_S' = V_1 - \frac{(V_2 - V_1)}{(L_2 - L_1)} L_1 \quad (1)$$

$$V_D' = V_2 + \frac{(V_2 - V_1)}{(L_2 - L_1)} (L - L_2) \quad (2)$$

where L_1 , L_2 , and L are the lengths from the source to the first sense probe, the second sense probe, and the drain, respectively.⁴⁰⁻⁴² The source resistance R_S , the drain resistance R_D , and the channel resistance R_{Ch} are estimated from the voltage drops at the source $\Delta V_S = V_S'$ and the drain $\Delta V_D = V_D - V_D'$ as follows

$$R_S = \Delta V_S / I_D \quad (3)$$

$$R_D = \Delta V_D / I_D \quad (4)$$

$$R_{Ch} = R_T - (R_S + R_D) \quad (5)$$

where R_T is the total resistance.^{41,42,46}

Figures 3(b) and 3(c) show V_G dependence of the potentials at the source V_S' , sense probes V_1 and V_2 , and drain V_D' . At $V_D = -5$ V (Fig. 3(b)), the voltage drop at the source ΔV_S amounts to 75 % of the total V_D at $V_G = -30$ V, which, however, reduces to 24% at $V_G = -50$ V. At $V_D = -15$ V (Fig. 3(c)), ΔV_S is as large as the voltage drop at the drain ΔV_D , which is approximately one third of the overall resistance. In general, ΔV_S is remarkably large in the subthreshold region, but usually ΔV_S and ΔV_D are $\sim 25\%$ of the total resistance. These results are consistent with the well-known four-probe and transfer-line observations as well as theoretical simulation in which the contact resistance diverges in the subthreshold region.^{41,42,47,48}

In the ordinary two-probe (2P) measurement, the contact effect potentially introduces critical errors in estimating the carrier mobility μ_{in}^{2P} . The four-probe method (4P) enables the estimation of contact-corrected mobility μ_{in}^{4P} . In the linear regime ($V_G \gg V_D + V_T$), I_D is directly proportional to V_D , and written as

$$I_D = \frac{W}{L} \sigma_{2P} V_D \quad (6)$$

$$I_D = \frac{W}{L/3} \sigma_{4P} V_{12} \quad (7)$$

in the 2P and 4P measurements, respectively, where σ is the field-effect conductivity

$$\sigma = \mu C(V_G - V_T). \quad (8)$$

Accordingly, $\mu_{\text{lin}}^{4\text{P}}$ is evaluated to be $18 \text{ cm}^2/\text{Vs}$ from R_{Ch} at $V_D = -5 \text{ V}$ and $V_G = -45 \text{ V}$, although the corresponding $\mu_{\text{lin}}^{2\text{P}}$ is $10 \text{ cm}^2/\text{Vs}$ from R_T , which is smaller than the saturation mobility $\mu_{\text{sat}}^{2\text{P}}$ of $13 \text{ cm}^2/\text{Vs}$. Here, we have calculated $V_T = -30 \text{ V} \sim -36 \text{ V}$ from the conventional saturation regime method, because transfer characteristics measured at $V_D = -5 \text{ V}$ in the small V_G region are in the saturation regime.

D. Temperature dependence of the transfer characteristics

Variable temperature characteristics of transfer curves are depicted in Fig. 4. As the temperature is lowered from 290 K to 70 K, I_D *decreases* in the subthreshold region, but *increases* (as band-like) above $-V_G = 46 \text{ V}$ particularly at $V_D = -5 \text{ V}$ (Fig. 4(a) and 4(b)). In our previous measurements for C8BTBT crystals,³⁰ the subthreshold decrease was not obvious. The present crystalline film is slightly more disordered than the C8BTBT crystal, but we can discuss the band-like transport at large V_G after the shallow traps are entirely filled. The apparently decreasing I_D is, however, partly due to the negative shift of V_T (Fig. 4(a) and 4(c)), which may come from the increasing contact resistance at low temperatures.⁴³ At 60 K, I_D drops abruptly, but I_D increases again below this temperature. At the same time, V_T shifts to the *positive* direction. I_D potentially suffers from the extrinsic effect of the V_T shift particularly in the subthreshold region, but I_D at 60 K certainly drops at $V_G = -50 \text{ V}$ in spite of the positive V_T shift. I_D in the high V_G region represents the comparatively intrinsic properties.

Accordingly, the two-probe (2P) mobility in the linear regime $\mu_{\text{lin}}^{2\text{P}}$ is estimated (Eq. 8) at $V_G = -45 \text{ V}$ and $V_D = -5 \text{ V}$ (Fig. 5(a)). $\mu_{\text{lin}}^{2\text{P}}$ increases from $10 \text{ cm}^2/\text{Vs}$ to $15 \text{ cm}^2/\text{Vs}$ when the sample is cooled from 290 K to 70 K. The 2P mobility in the saturation regime $\mu_{\text{sat}}^{2\text{P}}$

calculated from the square root plot of I_D at $V_D = -15$ V shows similar band-like characteristics, which increases from $13 \text{ cm}^2/\text{Vs}$ (290 K) to $20 \text{ cm}^2/\text{Vs}$ (70 K). The high mobility values of μ_{lin}^{2P} and μ_{sat}^{2P} are maintained down to 70 K. At 60 K, both μ_{lin}^{2P} and μ_{sat}^{2P} drop abruptly by 50%, but increases again below this temperature. The drop is similar to the organic single-crystal transistors using C8-BTBT, though no shoulder structure appears in the transfer curve.³⁰

The ideal trap-free transistor shows the $I_D \sim V_G^2$ dependence in the saturated region, but the exponent deviates from two like $I_D \sim (V_G - V_T)^\gamma$ due to the charge traps. Assuming the exponential trap distribution with the characteristic distribution width T_G

$$N(E) = N_G \exp(-E/kT_G) \quad (9)$$

where k is the Boltzmann constant and E is the energy measured from the conduction band edge,^{32,33,49,50} γ is represented by $T_G/T + 1$, and tends to be more than two. The γ values are estimated as slopes from the double logarithmic plot of transfer curves measured at $V_D = -15$ V (Fig. 5(b)). The transfer characteristics follows the power law very well, and the γ value is almost two in the whole temperature range (Fig. 5(c)), indicating ideal trap-free transistor characteristics. Similar phenomenon has been reported in high-mobility conjugated polymers.⁵⁰

E. 4P Analysis of the low-temperature anomaly

Figure 5(d) shows temperature dependence of the overall resistance (V_D/I_D), the resistance up to the sense probes ($(V_D - V_1)/I_D$ and $(V_D - V_2)/I_D$), and the resistance up to the insides of the source and the drain electrodes ($(V_D - V_S')/I_D$ and $(V_D - V_S'')/I_D$) measured from V_D . Here, the potentials are measured from V_D similarly to Fig. 3 in order to remove the influence of R_S . Since V_D is a constant, all potentials are divided by I_D , and the vertical axis

represents the temperature variation of the resistance. A representative result at $V_D = -45$ V and $V_D = -5$ V is depicted, but other plots show basically similar properties.

The uppermost curve (V_D/I_D) represents the total resistance, and shows an abrupt jump at 60 K. The potentials at the sense probes do not suffer from the anomaly, and the channel resistance R_{Ch} is continuous down to low temperatures. The drain resistance R_D is also continuous, and the jump solely comes from the source resistance R_S . The elimination of the R_S anomaly is universally observed in other V_G and V_D combinations. Except for the anomaly, R_S increases at high temperatures but becomes nearly constant at low temperatures in agreement with the theoretical prediction.⁴⁸

The four-probe (4P) mobility μ_{in}^{4P} is estimated by putting R_{Ch} in Eq. 8 (Fig. 5(a)). In the large V_G region, I_D increases with decreasing the temperature down to 70 K (Fig. 4(c)), and μ_{in}^{4P} increases by following the conventional power law $\mu \sim T$ of the band-like transport.⁵¹ The 4P mobility amounts to 45 cm²/Vs at 70 K. This large value stems from a small $(V_2 - V_1)/I_D \sim 7$ k Ω (between the black curves) in Fig. 5(d). The drop at 60 K is mostly eliminated in μ_{in}^{4P} , though μ_{in}^{4P} still decreases below this temperature. Probably, the decreasing μ_{in}^{4P} is not intrinsic but due to the incomplete elimination of the 60 K contact anomaly, because constant V_D condition is applied to the non Ohmic transistor characteristics. Nonetheless, we can conclude the 60 K anomaly mainly comes from R_S .

IV. CONCLUSION

We have investigated organic single-crystal transistors using Ph-BTBT-C10 by the four-probe measurement. A single crystalline film of Ph-BTBT-C10 having a large domain is fabricated by the blade-coating method. The resulting transistor exhibits as large μ_{in}^{4P} as 18 cm²/Vs at room temperature, though the contribution of the contact resistance is significant. It is not surprising because in general, the contribution of contact resistance becomes large in

high-mobility transistors with small channel resistance. At small $V_D = -5\text{V}$, the voltage drop at the source contact is significant in the subthreshold region, although R_S decreases by applying V_G . At large $V_D = -15\text{ V}$, the voltage drop at the source is one third of V_D in the entire V_G region, and the drop at the drain is comparatively large due to the formation of the pinch-off zone in the saturation regime.

In the variable temperature measurements, μ^{2P} increases with decreasing the temperature down to 70 K, and band-like transport is observed. The saturation regime I_D follows the ideal transistor formula of $I_D \sim (V_G - V_T)^2$, reflecting comparatively trap-free nature of the present transistor. An abrupt mobility drop is observed at 60 K, but band-like transport is restored again down to 30 K. The abrupt drop is mostly eliminated in the 4P measurement, indicating the drop comes from the source resistance.

In bulk conductors, the four-probe measurement is a common method, and in metallic conductors, it happens frequently that the contact resistance is by several orders larger than the bulk resistance. In field-effect transistors, the four-probe measurement is carried out in exceptional cases, but the present result demonstrates the contact effect is significant in high-performance single-crystal transistors. In such a case, we can expect μ_{lin}^{4P} more than three times larger than μ_{lin}^{2P} . It is noteworthy that the source resistance and the drain resistance contribute differently depending on V_G and temperature, and sometimes give remarkable anomaly in μ_{lin}^{2P} . However, the anomaly is eliminated in the 4P measurement, and the intrinsic charge transport in the present blade-coated organic semiconductor is regarded as essentially band-like down to the liquid helium temperatures as observed in the time-of-flight measurement.³¹

ACKNOWLEDGEMENTS

Blade-coating of organic semiconductors and fabrication of the organic transistors were carried out at Flexible Electronics Research Center, National Institute of Advanced Industrial Science and Technology (AIST) in Tsukuba, Japan. We would like to thank to Prof. T. Hasegawa for his kind guidance to the experiments and the financial supports. We also thank to H. Minemawari, H. Watanabe, T. Yamada, S. Inoue, J. Tsutsumi, and S. Arai for the Ph-BTBT-10 sample and their helpful supports.

1. Briseno, A. L. *et al.* Patterning organic single-crystal transistor arrays. *Nature* **444**, 913–7 (2006).
2. Diao, Y. *et al.* Solution coating of large-area organic semiconductor thin films with aligned single-crystalline domains. *Nat. Mater.* **12**, 665–71 (2013).
3. Li, Y. *et al.* Flexible field-effect transistor arrays with patterned solution-processed organic crystals. *AIP Adv.* **3**, 052123 (2013).
4. Pierre, A. *et al.* All-Printed Flexible Organic Transistors Enabled by Surface Tension-Guided Blade Coating. *Adv. Mater.* **26**, 5722–7 (2014).
5. Uemura, T., Hirose, Y., Uno, M., Takimiya, K. & Takeya, J. Very High Mobility in Solution-Processed Organic Thin-Film Transistors of Highly Ordered [1]Benzothieno[3,2-b]benzothiophene Derivatives. *Appl. Phys. Express* **2**, 111501 (2009).
6. Minemawari, H. *et al.* Inkjet printing of single-crystal films. *Nature* **475**, 364–7 (2011).
7. Giri, G., Park, S., Vosgueritchian, M., Shulaker, M. M. & Bao, Z. High-mobility, aligned crystalline domains of TIPS-pentacene with metastable polymorphs through lateral confinement of crystal growth. *Adv. Mater.* **26**, 487–93 (2014).
8. Dong, H., Fu, X., Liu, J., Wang, Z. & Hu, W. 25th anniversary article: key points for high-mobility organic field-effect transistors. *Adv. Mater.* **25**, 6158–83 (2013).
9. Zhao, Y., Guo, Y. & Liu, Y. 25th anniversary article: recent advances in n-type and ambipolar organic field-effect transistors. *Adv. Mater.* **25**, 5372–91 (2013).
10. Zaumseil, J. & Sirringhaus, H. Electron and ambipolar transport in organic field-effect transistors. *Chem. Rev.* **107**, 1296–323 (2007).
11. Sheraw, C. D., Jackson, T. N., Eaton, D. L. & Anthony, J. E. Functionalized Pentacene Active Layer Organic Thin-Film Transistors. *Adv. Mater.* **15**, 2009–2011 (2003).
12. Ebata, H. *et al.* Highly soluble [1]benzothieno[3,2-b]benzothiophene (BTBT) derivatives for high-performance, solution-processed organic field-effect transistors. *J. Am. Chem. Soc.* **129**, 15732–3 (2007).
13. Yuan, Y. *et al.* Ultra-high mobility transparent organic thin film transistors grown by an off-centre spin-coating method. *Nat. Commun.* **5**, 3005 (2014).
14. Izawa, T., Miyazaki, E. & Takimiya, K. Molecular Ordering of High-Performance Soluble Molecular Semiconductors and Re-evaluation of Their Field-Effect Transistor Characteristics. *Adv. Mater.* **20**, 3388–3392 (2008).
15. Iino, H., Usui, T. & Hanna, J.-I. Liquid crystals for organic thin-film transistors. *Nat. Commun.* **6**, 6828 (2015).
16. Inoue, S. *et al.* Effects of Substituted Alkyl Chain Length on Solution-Processable Layered Organic Semiconductor Crystals. *Chem. Mater.* **27**, 3809–3812 (2015).
17. Minemawari, H. *et al.* Crystal structure of asymmetric organic semiconductor 7-decyl-2-phenyl[1]benzothieno[3,2-b][1]benzothiophene. *Appl. Phys. Express* **7**, 091601 (2014).

18. Gershenson, M. E., Podzorov, V. & Morpurgo, A. F. Colloquium: Electronic transport in single-crystal organic transistors. *Rev. Mod. Phys.* **78**, 973–989 (2006).
19. Lezama, I. G. & Morpurgo, A. F. Progress in organic single-crystal field-effect transistors. *MRS Bull.* **38**, 51–56 (2013).
20. Podzorov, V. Organic single crystals: Addressing the fundamentals of organic electronics. *MRS Bull.* **38**, 15–24 (2013).
21. Podzorov, V. *et al.* Intrinsic Charge Transport on the Surface of Organic Semiconductors. *Phys. Rev. Lett.* **93**, 086602 (2004).
22. Hulea, I. N. *et al.* Tunable Fröhlich polarons in organic single-crystal transistors. *Nat. Mater.* **5**, 982–6 (2006).
23. Zimmerling, T. & Batlogg, B. Improving charge injection in high-mobility rubrene crystals: From contact-limited to channel-dominated transistors. *J. Appl. Phys.* **115**, 164511 (2014).
24. Minder, N. A. *et al.* Tailoring the Molecular Structure to Suppress Extrinsic Disorder in Organic Transistors. *Adv. Mater.* **26**, 1254 (2014).
25. Krupskaya, Y., Gibertini, M., Marzari, N. & Morpurgo, A. F. Band-Like Electron Transport with Record-High Mobility in the TCNQ Family. *Adv. Mater.* **27**, n/a–n/a (2015).
26. Sakanoue, T. & Sirringhaus, H. Band-like temperature dependence of mobility in a solution-processed organic semiconductor. *Nat. Mater.* **9**, 736–40 (2010).
27. Uemura, T. *et al.* Band-like transport in solution-crystallized organic transistors. *Curr. Appl. Phys.* **12**, S87–S91 (2012).
28. Liu, C. *et al.* Solution-processable organic single crystals with bandlike transport in field-effect transistors. *Adv. Mater.* **23**, 523–6 (2011).
29. Matsubara, K., Manaka, T. & Iwamoto, M. Band-like transport observed in TIPS-pentacene thin film by time-resolved microscopic optical second-harmonic generation imaging. *Appl. Phys. Express* **8**, 041601 (2015).
30. Cho, J., Higashino, T. & Mori, T. Band-like transport down to 20 K in organic single-crystal transistors based on dioctylbenzothienobenzothiophene. *Applied Physics Letters* **106**, 193303 (2015).
31. Warta, W. & Karl, N. Hot holes in naphthalene: High, electric-field-dependent mobilities. *Phys. Rev. B* **32**, 1172–1182 (1985).
32. Akiyama, Y. & Mori, T. Analysing organic transistors based on interface approximation. *AIP Adv.* **4**, 017126 (2014).
33. Cho, J., Akiyama, Y., Kakinuma, T. & Mori, T. Trap density of states in n-channel organic transistors: variable temperature characteristics and band transport. *AIP Adv.* **3**, 102131 (2013).
34. Newman, C. R., Chesterfield, R. J., Merlo, J. A. & Frisbie, C. D. Transport properties of single-crystal tetracene field-effect transistors with silicon dioxide gate dielectric. *Appl. Phys. Lett.* **85**, 422 (2004).

35. Takeya, J. *et al.* Field-induced charge transport at the surface of pentacene single crystals: A method to study charge dynamics of two-dimensional electron systems in organic crystals. *J. Appl. Phys.* **94**, 5800 (2003).
36. Xie, H., Alves, H. & Morpurgo, A. F. Quantitative analysis of density-dependent transport in tetramethyltetraselenafulvalene single-crystal transistors: Intrinsic properties and trapping. *Phys. Rev. B* **80**, 245305 (2009).
37. Minder, N. A., Ono, S., Chen, Z., Facchetti, A. & Morpurgo, A. F. Band-like electron transport in organic transistors and implication of the molecular structure for performance optimization. *Adv. Mater.* **24**, 503–8 (2012).
38. Xie, W. *et al.* Temperature-independent transport in high-mobility dinaphtho-thienothiophene (DNNT) single crystal transistors. *Adv. Mater.* **25**, 3478–84 (2013).
39. Kanicki, J. Gated-four-probe a-Si:H TFT structure: a new technique to measure the intrinsic performance of a-Si:H TFT. *IEEE Electron Device Lett.* **18**, 340–342 (1997).
40. Richards, T. J. & Sirringhaus, H. Analysis of the contact resistance in staggered, top-gate organic field-effect transistors. *J. Appl. Phys.* **102**, 094510 (2007).
41. Chesterfield, R. J. *et al.* Variable temperature film and contact resistance measurements on operating n-channel organic thin film transistors. *J. Appl. Phys.* **95**, 6396 (2004).
42. Pesavento, P. V., Chesterfield, R. J., Newman, C. R. & Frisbie, C. D. Gated four-probe measurements on pentacene thin-film transistors: Contact resistance as a function of gate voltage and temperature. *J. Appl. Phys.* **96**, 7312 (2004).
43. Zojer, K., Zojer, E., Fernandez, A. F. & Gruber, M. Impact of the Capacitance of the Dielectric on the Contact Resistance of Organic Thin-Film Transistors. *Phys. Rev. Appl.* **4**, 044002 (2015).
44. Necliudov, P. V., Shur, M. S., Gundlach, D. J. & Jackson, T. N. Contact resistance extraction in pentacene thin film transistors. *Solid. State. Electron.* **47**, 259–262 (2003).
45. Gruber, M., Zojer, E., Schürer, F. & Zojer, K. Impact of Materials versus Geometric Parameters on the Contact Resistance in Organic Thin-Film Transistors. *Adv. Funct. Mater.* **23**, 2941–2952 (2013).
46. Weis, M., Manaka, T. & Iwamoto, M. Origin of electric field distribution in organic field-effect transistor: Experiment and analysis. *J. Appl. Phys.* **105**, 024505 (2009).
47. Xu, Y. *et al.* Modified transmission-line method for contact resistance extraction in organic field-effect transistors. *Appl. Phys. Lett.* **97**, 063302 (2010).
48. Gruber, M., Schürer, F. & Zojer, K. Relation between injection barrier and contact resistance in top-contact organic thin-film transistors. *Org. Electron.* **13**, 1887–1899 (2012).
49. Kronemeijer, A. J. *et al.* Two-Dimensional Carrier Distribution in Top-Gate Polymer Field-Effect Transistors: Correlation between Width of Density of Localized States and Urbach Energy. *Adv. Mater.* **26**, 728–33 (2014).
50. Venkateshvaran, D. *et al.* Approaching disorder-free transport in high-mobility conjugated polymers. *Nature* **515**, 384–388 (2014).

51. Troisi, A. & Orlandi, G. Charge-Transport Regime of Crystalline Organic Semiconductors: Diffusion Limited by Thermal Off-Diagonal Electronic Disorder. *Phys. Rev. Lett.* **96**, 086601 (2006).

Figure captions

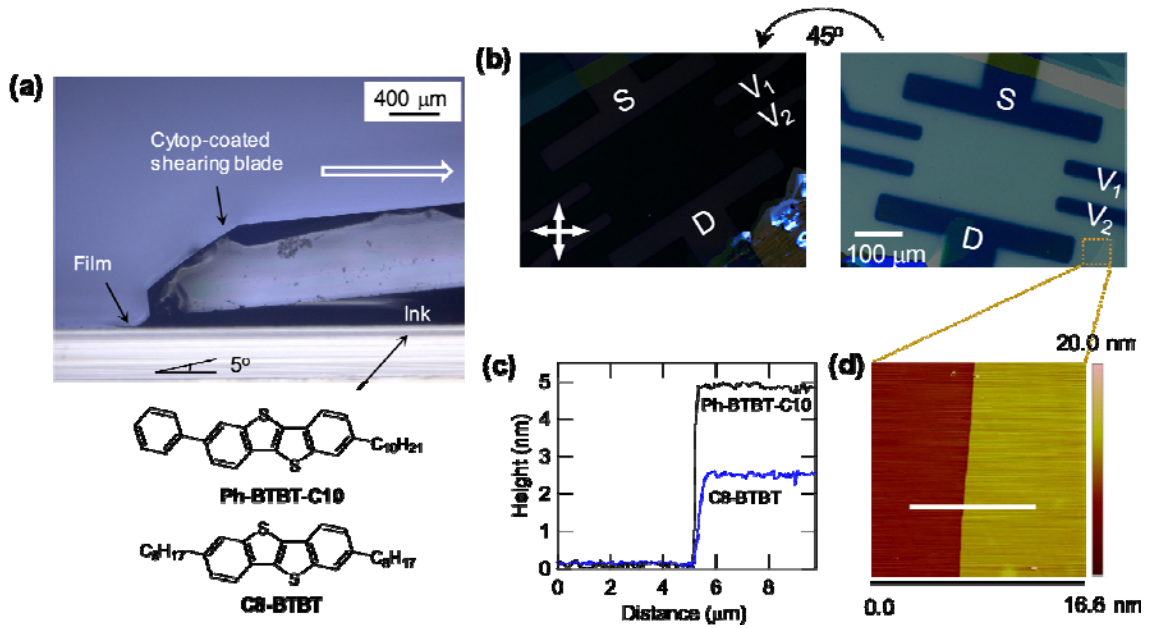


FIG. 1. (a) An optical image of the blade-coating system. The white arrow indicates the shearing direction. The chemical structures of semiconductor inks, Ph-BTBT-C10 and C8-BTBT, are shown at the bottom. (b) Cross-nicols polarized optical micrographs of the Ph-BTBT-C10 film with Au contacts for the four-probe measurement with sense probes (V_1 and V_2). (c) Height of step structures measured by AFM. (d) AFM image of a step-and-terrace structure found on the crystalline film shown in (b).

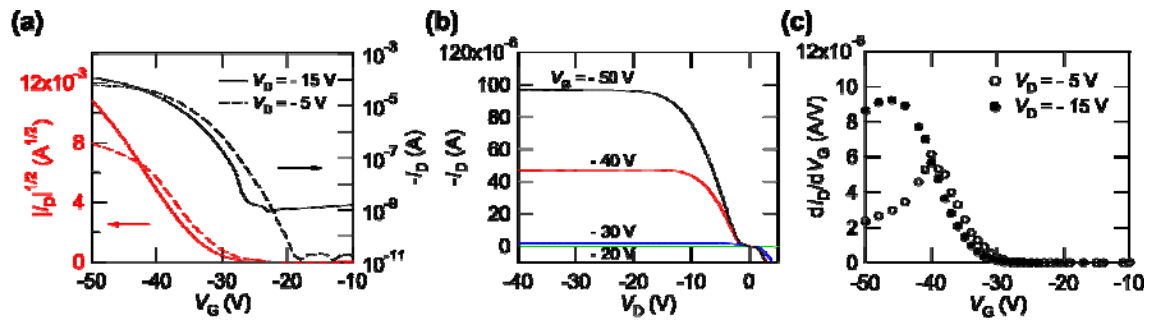


FIG. 2. (a) Transfer, and (b) output characteristics, and (c) transconductance dI_D/dV_G of an organic single-crystal transistor based on Ph-BTBT-C10 at 290 K.

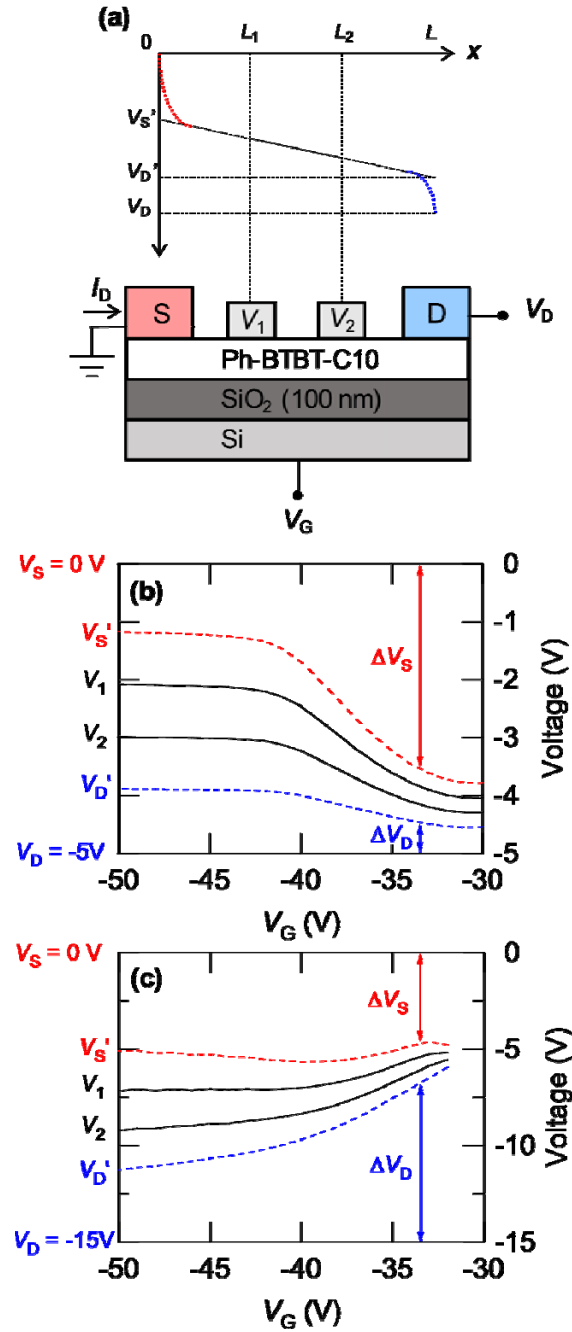


FIG. 3. (a) Schematic image of the organic transistor with four-probe configuration and the voltage profile in the channel. Four-probe results as a function of V_G at (b) $V_D = -5V$ and (c) $V_D = -15V$, measured at room temperature. V_1 and V_2 are potentials at the sense probes. V_S' and V_D' are the potentials just inside of the source and drain contacts estimated by the linear extrapolation from the sense probes. ΔV_S and ΔV_D are voltage drops at the source and drain contacts. Note that the total voltage drop is always $V_D = -5V$ or $-15V$.

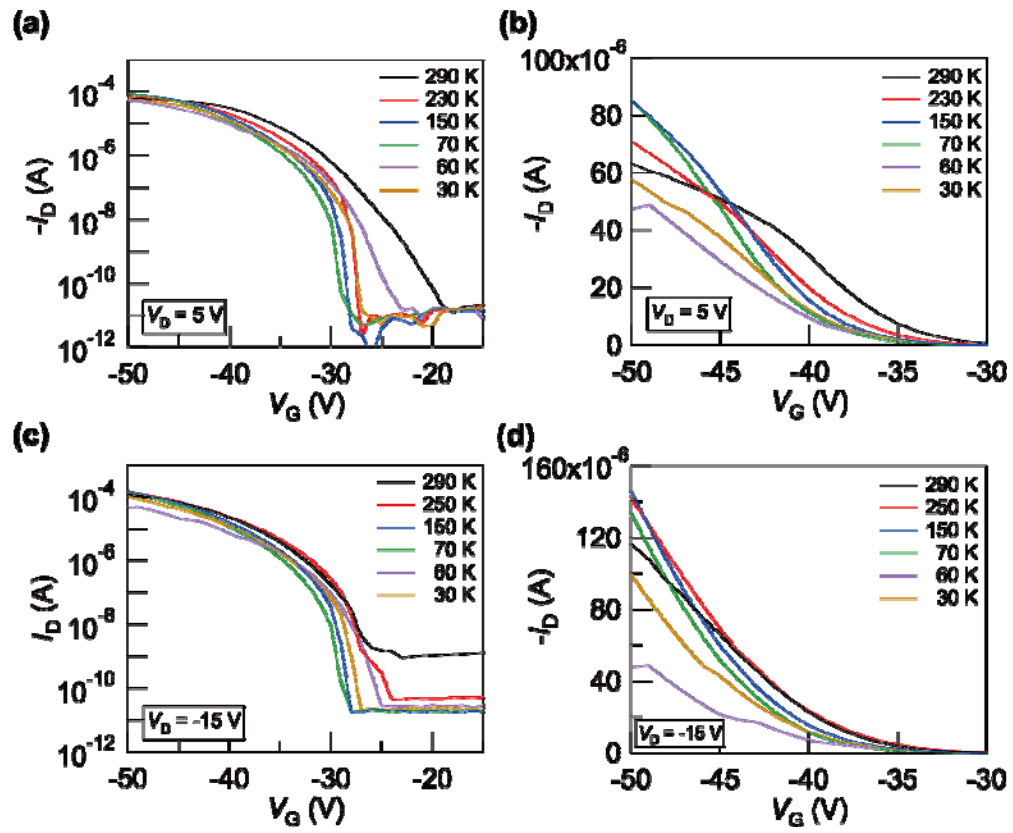


FIG. 4. Transfer characteristics at $V_D = -5$ V on (a) a logarithmic scale, and (b) a linear scale.

Transfer characteristics at $V_D = -15$ V on (c) a logarithmic scale, and (d) a linear scale.

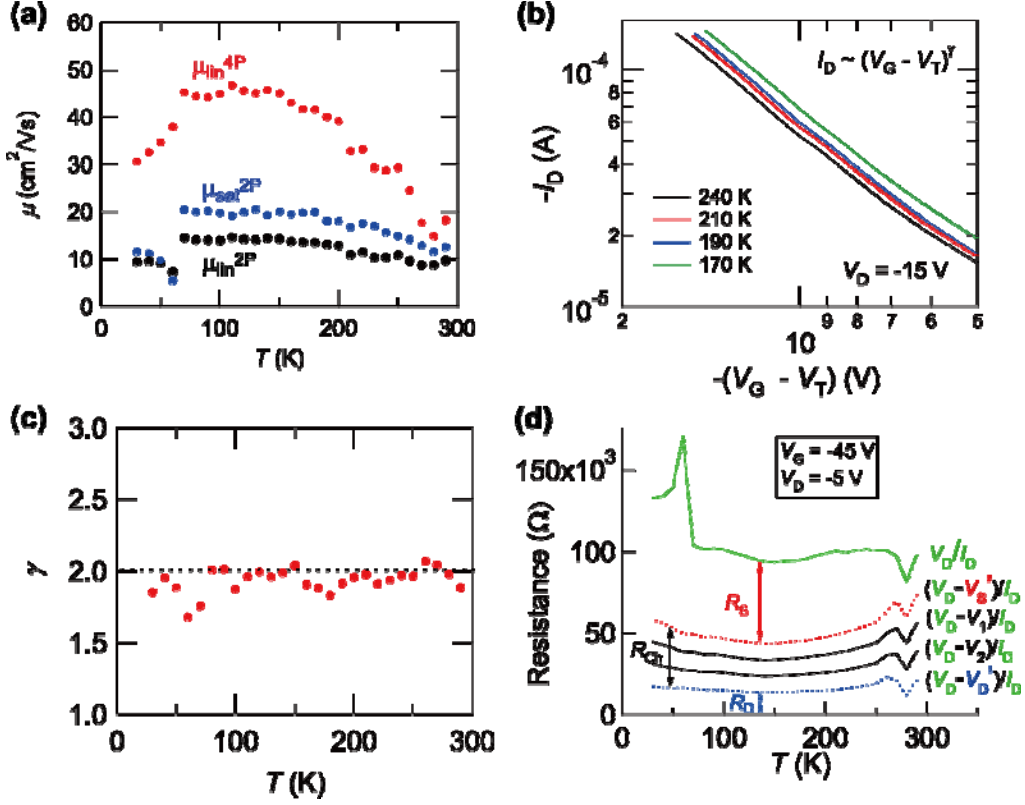


FIG. 5. (a) Temperature dependence of two-probe (μ_{lin}^{2P} , black) and four-probe (μ_{lin}^{4P} , red) linear mobility extracted at $V_D = -5$ V, and saturation mobility (μ_{sat}^{2P} , blue) estimated at $V_D = -15$ V. (b) Variable-temperature transfer characteristics at $V_D = -15$ V are plotted on the double logarithmic scale to extract the parameter γ . (c) Temperature dependence of γ . (d) Four-probe results as a function of temperature at $V_G = -45$ V and $V_D = -5$ V. The overall resistance (V_D/I_D), the resistance up to the sense probes ($(V_D - V_1)/I_D$ and $(V_D - V_2)/I_D$), and the resistance up to the insides of the source and the drain electrodes ($(V_D - V_{S'})/I_D$ and $(V_D - V_{S''})/I_D$) measured from V_D , are plotted to show the potential distribution and the temperature dependence of the source (R_S), channel (R_{Ch}), and drain resistance (R_D).